DOI: 10.1002/ ((please add manuscript number))
**Article type:** Full Paper

# Enhancing Oxygen Reduction Activity and Cr Tolerance of Solid Oxide Fuel Cell Cathodes by a Multi-phase Catalyst Coating

*Yinghua Niu[†], Yucun Zhou[†], Weiqiang Lv[†], Yu Chen*, Yanxiang Zhang, Weilin Zhang, Zheyu Luo, Nicholas Kane, Yong Ding, Luke Soule, Yuchen Liu, Weidong He*, Meilin Liu**

Yinghua Niu, Dr. Y. Zhou, Weilin Zhang, Zheyu Luo, Nicholas Kane, Dr. Yong Ding, Luke Soule, Yuchen Liu, Prof. M. Liu
School of Materials Science and Engineering, Center for Innovative Fuel Cell and Battery Technologies, Georgia Institute of Technology, Atlanta, GA, 30332-0245 USA
E-mail: meilin.liu@mse.gatech.edu
Yinghua Niu, Dr. Weiqiang Lv, Dr. Weidong He
School of Physics, University of Electronic Science and Technology of China, Chengdu, 610054, China
E-mail: weidong.he@uestc.edu.cn
Dr. Yu Chen
School of Environment and Energy, South China University of Technology, Guangzhou, 510006, China
E-mail: eschenyu@scut.edu.cn
Dr. Yanxiang Zhang
National Key Laboratory for Precision Hot Processing of Metals, MIIT Key Laboratory of Advanced Structure-Function Integrated Materials and Green Manufacturing Technology, School of Materials Science and Engineering, Harbin Institute of Technology, Harbin, 150001, China
Dr. Weidong He
National Key Laboratory of Science and Technology on Advanced Composites in Special Environments, and Center for Composite Materials and Structures, Harbin Institute of Technology, Harbin 150080, China
† These authors contributed equally to this work.

**Keywords:** Multi-phase catalyst, Oxygen reduction reaction, Solid oxide fuel cell, Cr tolerance, Cathode

Intermediate temperature solid oxide fuel cells (IT-SOFCs) are cost-effective and efficient energy conversion systems. The sluggish oxygen reduction reaction (ORR) and the degradation of cathodes are critical challenges to the commercialization of IT-SOFCs. Here we report a highly efficient multi-phase (MP) catalyst coating, consisting of $Ba_{1-x}Co_{0.7}Fe_{0.2}Nb_{0.1}O_{3-\delta}$ (BCFN) and

$BaCO_3$, to enhance the ORR activity and durability of the state-of-the-art $La_{0.6}Sr_{0.4}Co_{0.2}Fe_{0.8}O_3$ (LSCF) cathode. The conformal MP catalyst coated LSCF cathode shows a polarization resistance ($R_p$) of 0.048 Ω $cm^2$ at 650 °C, about one order of magnitude smaller than that of the bare LSCF (0.434 Ω $cm^2$). In an accelerated Cr-poisoning test (exposed to air with 3 vol.% water vapor), the degradation rate of the catalyst-coated LSCF electrode is $10^{-3}$ Ω $cm^2$ $h^{-1}$ within 200 hours, only one fifth of that for the bare LSCF electrode at 750 °C. In addition, anode-supported single cells with the MP catalyst-coated LSCF cathode show a dramatically enhanced peak power density (1.4 W $cm^{-2}$ versus 0.67 W $cm^{-2}$ at 750 °C) and durability against Cr and $H_2O$ (degradation rate of 0.05% $h^{-1}$ versus ~0.13% $h^{-1}$ at 0.25 A $cm^{-2}$ at 650 °C) than those of the cells with a bare LSCF cathode. Both experiments and density functional theory-based calculations indicate that the BCFN phase improves the ORR activity whereas the $BaCO_3$ phase enhances the stability of the LSCF cathode.

## 1. Introduction

Intermediate temperature solid oxide fuel cells (IT-SOFCs) are very promising energy conversion devices to directly convert the chemical energy from a wide variety of fuels (e.g., hydrogen and methane) to electricity.[1, 2] However, the performance and durability (mainly determined by the cathodes) of IT-SOFCs should be further enhanced to meet the commercial requirements.[3, 4] Lanthanum strontium cobalt ferrite (LSCF) is the most widely investigated and representative cathode materials for IT-SOFCs due to the high mixed ionic and electronic conductivities, adequate electrochemical activity, and compatible thermal expansion coefficient (CTE) with other cell components.[5, 6] One of the main challenges for the practical application of LSCF is the surface SrO segregation/enrichment driven by the electrostatic and elastic interactions under fuel cell

operating conditions.[7-9] The Sr segregation alters the structure and composition of LSCF and is detrimental to the electro-catalytic activity and durability.[10, 11] Moreover, segregated SrO readily reacts with vaporized Cr species (e.g., $CrO_3$ and $CrO_2(OH)_2$) from Cr-containing alloy interconnects and other components in the SOFC system to form insulating $SrCrO_4$ and $Cr_2O_3$ solid phases through a nucleation, crystallization, and grain growth process.[12-14] The formed inert secondary phases on the surface of LSCF disrupt electron conduction as well as surface oxygen transport and dissociation, resulting in an increase in Ohmic resistance and a decrease in electrocatalytic activity for oxygen reduction reaction (ORR).[15-17] The Sr segregation and Cr poisoning effect will be significantly exacerbated by the presence of $H_2O$.[18-21]

Surface modification by catalyst coatings has been demonstrated as an effective strategy to enhance the ORR activity and contaminants tolerance of cathodes.[22-27] The catalyst coatings can provide ORR active sites and protect LSCF from contacting with contaminates. [18, 21, 28-31] Several types of catalysts have been developed, including precious metals (e.g., Pd, Ag, and Ru), oxygen ion-conducting oxides ($Sm_{0.2}Ce_{0.8}O_{2-\delta}$ (SDC),[31, 32] $Gd_{0.2}Ce_{0.8}O_{1.9}$),[31, 33] mixed ionic and electronic conductors (e.g., LSCF,[34] $Sm_{0.5}Sr_{0.5}CoO_{3-\delta}$,[34] and $PrSrCoMnO_{6-\delta}$[23] *etc*.), and Ba-containing compounds (BaO,[24] $BaCO_3$ [35]). The high cost and rapid degradation due to contaminations (e.g., CO and $H_2S$) of precious metals limit their applications.[36] Oxides coated cathodes normally suffer from high polarization resistances (>0.15 **Ω** $cm^2$ at 650 ºC).[37, 38] In addition, most of the catalysts exist in the form of isolated particles on the surface of cathodes, which cannot effectively suppress Sr segregation and Cr poisoning.[35]

Recently, Chen *et al*.[39] fabricated a hybrid catalyst coating composed of a conformal $PrNi_{0.5}Mn_{0.5}O_3$ (PNM) thin film with exsolved $PrO_x$ nanoparticles on the surface of the LSCF cathode by a facile solution infiltration process. As reported, the rate of electron transfer for ORR

could be greatly accelerated by the oxygen-vacancy-rich surfaces of the $PrO_x$ nanoparticles while the oxide-ion transport could be enhanced by the PNM film.[39] More importantly, the hybrid coating is catalytically active for ORR but inert to contaminant poisoning. For example, when subjected to an accelerated Cr-poisoning test, the cell with a catalyst-coated LSCF cathode showed a significantly enhanced durability (degradation rate of 0.0434% $h^{-1}$ at 0.7 V and 750 °C) compared to the cell with a bare LSCF cathode (degradation rate of 0.4% $h^{-1}$ at 0.7 V and 750 °C).[18] Very recently, a multi-phase (MP) catalyst coating which is composed of $BaCoO_{3-x}$ (BCO)-$PrCoO_{3-x}$ (PCO) nanoparticles (NPs) and a conformal $PrBa_{0.8}Ca_{0.2}Co_2O_{5+\delta}$ (PBCC) thin film was designed to dramatically enhance the ORR kinetics of the LSCF cathode.[40] It is generally believed that the conformal coating has better durability and contaminants tolerance than the isolated nanoparticles coating since the former can cover the entire cathode surface and avoid the coarsening issue of nanoparticles. [18, 41]

In this article, we report a rationally designed $Ba_{1-x}Co_{0.7}Fe_{0.2}Nb_{0.1}O_{3-\delta}$ (BCFN)-$BaCO_3$ MP catalyst for the state-of-the-art LSCF cathode, which can be readily fabricated via a one-step infiltrating process. The conformal MP catalyst coating significantly enhanced the ORR activity and contaminants (i.e., Cr and $H_2O$) tolerance of the LSCF cathode (**Figure 1**). The MP catalyst-coated LSCF cathode exhibited a minimal polarization resistance ($R_p$) of 0.048 Ω $cm^2$ at 650 ˚C, which is almost one order of magnitude smaller than that of the bare LSCF cathode (0.434 Ω $cm^2$). In addition, the degradation rate of the catalyst-coated LSCF was $10^{-3}$ Ω $cm^2$ $h^{-1}$ within a 200-hour Cr-poisoning test (exposed to air containing 3 vol.% $H_2O$), only one fifth of that for the bare LSCF electrode at 750 °C. The improved activity and stability of the MP catalyst-coated LSCF were verified in single cells under typical SOFC operating conditions. The excellent performance is attributed to a synergistic effect of the two separate phases, the BCFN phase to improve the ORR

activity and the $BaCO_3$ phase to enhance the contaminants tolerance, as confirmed by experimental measurements and theoretical calculations.

## 2. Results and Discussion

### 2.1. Morphology and Structure of the MP catalyst-coated LSCF

Scanning electron microscopy（SEM) images and energy dispersive spectroscopy (EDS) mapping of the MP catalyst-coated LSCF are shown in **Figure 2**a and **Figure 2**b, respectively, revealing a conformal coating with elements of Ba, Co, Fe, Nb, and C. **Figure 2**c shows the bright-field transmission electron microscopy (TEM) image of a LSCF grain coated by the MP catalyst with the coating thickness of 20 to 50 nm. In the selected area electron diffraction (SAED) patterns, the diffraction spots pointed by the arrows indicate the existence of grains on the surface of LSCF (**Figure 2**d). High-resolution TEM (HRTEM) images in **Figure 2**e suggest that the coating consists of BCFN and $BaCO_3$. **Figure 2**e(i) shows lattices with *d* spacings of 0.280 nm and 0.198 nm, corresponding to the (110) and (200) facets of cubic-structured BCFN, respectively. $BaCO_3$ is observed in the outer layer of the coating with a thickness of ~1.5 nm (**Figure 2**e), as evidenced by an average d-spacing of 0.378 nm for the (111) plane of orthorhombic $BaCO_3$ (**Figure 2**e(ii)). Further evidence of the formation and distribution of BCFN and $BaCO_3$ is provided by the electron energy-loss spectroscopy (EELS) spectra shown in **Figure 2**f, g. Ba $M_{5,4}$ and Co $L_{3,2}$ edges are observed throughout the coating layer, indicating a uniform distribution of BCFN. The C K edge is observed on the border of the coating (points A4 and B3), confirming that the $BaCO_3$ phase is on the surface of the coating (**Figure 2**e). The formation the $BaCO_3$ phase is also verified by the Raman spectroscopy (**Figure S1**). The crystal structure of the MP catalyst is further confirmed by X-ray diffraction (XRD) characterizations. Due to the low catalyst loading (7.5 wt.%, **Figure S2**a),

it's hard to analysis the catalyst patterns in a MP catalyst-coated LSCF electrode (**Figure S2**b). Instead, the MP catalyst powder prepared by calcinating the infiltration solution at 750 ˚C for 1 h was used for characterization. As shown in **Figure S2**c, main peaks of the MP catalyst can be indexed to the BCFN phase (PDF-04-018-5509) and $BaCO_3$ phase (PDF-00-045-1471).[42, 43] Typical nitrogen adsorption/desorption isotherm curves of bare LSCF and MP catalyst-coated LSCF electrodes are shown in **Figure S2**d. The observed type IV isotherm hysteresis indicates the formation of mesoporous network in the MP catalyst-coated LSCF.[44-46] The hysteresis for the MP catalyst-coated LSCF starts at a lower $P/P_0$ value as compared with that for the bare LSCF, indicating the micropores in MP catalyst-coated LSCF. The corresponding pore size distribution calculated by the Barret−Joyner−Halenda (BJH) method using the desorption branch is shown in the inset of **Figure S2**d. Both microspores and mesopores are observed in the MP catalyst-coated LSCF. The specific surface area of the catalyst-coated LSCF is 8.6 $m^2 g^{-1}$, about ten times higher than that of the bare LSCF electrode (0.8 $m^2 g^{-1}$).

### 2.2. Enhanced Activity of the MP catalyst-coated LSCF cathode

The MP catalyst is very active in reducing the polarization resistance of the LSCF cathode. As shown in **Figure 3**a, the MP catalyst-coated LSCF exhibits low Rp values of 0.015, 0.022, 0.049, and 0.175 Ω $cm^2$ at 750, 700, 650, and 600 ºC, respectively. Temperature dependence of Rp's of the bare LSCF and catalysts coated LSCF electrodes are shown in **Figure 3**b. The MP catalyst-coated LSCF cathode shows a smaller activation energy (1.26 eV) than that of the bare LSCF cathode (1.33 eV). Moreover, the MP catalyst-coated LSCF cathode shows a much smaller Rp when compared with the bare LSCF cathode (**Figure 3**b). At 650 ºC, for instance, the Rp of the MP catalyst-coated LSCF (0.048 Ω $cm^2$) is about one tenth of that of the bare LSCF (~4.3 Ω $cm^2$).

The MP catalyst is more active than the single-phase catalyst. For example, the Rp values of the $BaCO_3$, BCFN, and MP catalyst-coated LSCF cathode are 0.33, 0.26, and 0.048 Ω $cm^2$, respectively, at 600 ºC. It seems that the BCFN catalyst has a higher activity than $BaCO_3$. **Figure 3**b and **Table S1** compare the Rp values of our MP catalyst-coated LSCF cathode with other catalysts coated LSCF cathodes reported to date. As observed, the MP catalyst-coated LSCF shows the lowest Rp's at 600-750 ºC. To assess the effectiveness of the catalyst coating, a performance-improving factor ($f_P$) was adopted, which is defined as the ratio of the Rp for the bare LSCF to the Rp for the catalyst coated LSCF under the same conditions.[47] At 650 ºC, the MP catalyst-coated LSCF cathode reported in this work shows the largest $f_P$ among all catalyst-coated LSCF electrodes (**Table S1**), further confirming the high activity of the MP catalyst.

To gain a more insightful understanding of the kinetics of the electrochemical processes on the cathodes, distribution of relaxation time (DRT) of the impedance spectra is analyzed.[48] **Figure 3**c shows the DRT plots of the electrochemical processes for the bare LSCF and MP catalyst-coated LSCF cathodes at 750 °C in air. Each plot is composed of three distinct peaks observed in different frequency domains: high frequency (HF, >500 Hz), intermediate frequency (IF, ~10-500 Hz), and low frequency (LF, 0.1-10 Hz) range. Normally, the electrochemical processes contributed to the HF, IF, and LF peaks are associated, respectively, with charge transfer processes across electrolyte-cathode interfaces, surface oxygen exchange processes (e.g., oxygen adsorption, dissociation, and surface transport), and mass transfer processes (e.g., gas diffusion within the pores of the cathode, and the transport of ionic/electronic defects within the solid phase of the cathode).[40, 48] As shown in **Figure 3**c, the resistances in the HF and IF dominate the total polarization resistance of the bare LSCF cathode. By applying a MP catalyst, the resistances of the LSCF cathode in all the frequency range were greatly reduced, especially for the resistances in HF

and IF, indicating the accelerated charge transfer and surface oxygen exchange processes. Also shown in **Figure 3**c is the shift of the limiting step from the HF and IF-associated processes for the bare LSCF cathode to the LF-associated process for the MP catalyst-coated LSCF cathode.

Shown in **Figure 3**d and **Figure 3**e are the temperature dependence of the DRT functions and oxygen partial pressure ( $p_{O_2}$ ) dependence of the EIS of the MP catalyst-coated LSCF cathode, respectively. As observed, processes associated with the peaks in the HF and IF ranges are very sensitive to temperature but less sensitive to $p_{O_2}$ . In contrast, the processes associated with the LF range is independent of temperature but strongly affected by $p_{O_2}$ . Similar behavior is also observed in the bare LSCF cathode (**Figure S3**a,b). The ORR reaction at the cathode can be divided into several elementary steps, [49-51] and the rate determining steps can be determined by *n* values from the Rp dependence of the $p_{O_2}$ [52-54]

$$\mathrm{Rp} \propto (p_{O_2})^{-n} \qquad (1)$$

The rate-determining step can be ascribed as following: $n$ = 1, gas diffusion in the cathode; $n$ = 0.75, adsorption of $O_2$ molecules onto the surface; $n$ = 0.5, dissociation of the adsorbed molecular oxygen into atomic oxygen; $n$ = 0.25, solid-phase migration of oxide ions in the cathode; and $n$ = 0, diffusion of oxide ions from triple phase boundaries (TPBs) to the electrolyte, associated with a charge transfer process.[54, 55]

To separate the HF, IF, and LF arc resistances, EIS of the MP catalyst-coated LSCF electrode acquired at different $p_{O_2}$ were fitted by the equivalent circuit shown in **Figure S3**c. In which, L is the inductance of the lead wires, $R_{HF}$, $R_{IF}$, and $R_{LF}$ are the widths of HF, IF, and LF arcs, while $Q_H$, $Q_I$, and $Q_L$ are the constant phase elements for the HF, IF, and LF arcs, respectively. As shown in **Figure 3**f, *n* values for the $R_{HF}$, $R_{IF}$, and $R_{LF}$ are 0.13, 0.75, and 1.28, respectively. It indicates

that the HF arc might be correlated with the charge transfer process, the IF arc corresponds to the adsorption and dissociation of oxygen molecules, and the LF arc is likely associated with the mass transport process. Given that the $R_{LF}$ is much larger than $R_{HF}$ and $R_{IF}$ at an elevated temperature (>650 °C) but much smaller than $R_{HF}$ and $R_{IF}$ at a lower temperature (<650 °C) (**Figure 3**d), it can be concluded that, as the operation temperature is reduced, the rate determining steps for the ORR over the MP catalyst-coated LSCF cathode shift from the gas diffusion process to the charge transfer and surface oxygen exchange processes.

### 2.3. Enhanced Stability of the MP catalyst-coated LSCF cathode

The MP catalyst-coated LSCF cathode shows a dramatically enhanced stability when exposed to dry air, humidified air, and humidified air with Cr source. The catalyst loading and calcining temperature were optimized to be 15 μL of 0.1 M infiltration solution (~7.5wt.% of the bare cathode) and 750 °C (**Figure S4**). Durability of the MP catalyst-coated LSCF cathode was first investigated in air without the Cr source. As shown in **Figure 4**a (i), the Rp of the bare LSCF cathode increased with time while that of the MP catalyst-coated cathode remained constant in dry air. With the introduction of 3 vol.% $H_2O$, the degradation rate of the bare LSCF cathode increased from 0.57% $h^{-1}$ in dry air to 1.27% $h^{-1}$ in humidified air (**Figure 4**a (i)(ii)). However, no obvious degradation was observed in the Rp of the MP catalyst-coated cathode under humidified air (**Figure 4**a (ii)), indicating a high tolerance of the coating against water. In the presence of Cr source, an accelerated degradation is observed for the bare LSCF cathode; the degradation rate was increased from 1.7% $h^{-1}$ in dry air to 2.8% $h^{-1}$ in humidified air (**Figure 4**a (iii)(iv)). The degradation rate in humidified air is greater than that in dry air, attributed to the water-promoted Sr segregation of the LSCF cathode and the much higher Cr concentration in the humidified atmosphere.[20] As reported, the partial pressure of $CrO_2(OH)_2$ (~0.22 Pa) in wet air (3 vol.%$H_2O$)

is about 1,360 times higher than that of $CrO_3$ (~$1.6\times10^{-4}$ Pa ) in dry air at 750 °C.[48] In comparison, the MP catalyst-coated LSCF cathode is much more stable in the presence of Cr source. For instance, the Rp of the bare LSCF cathode increased by 0.2 Ω $cm^2$ over the 100-h test in dry air with Cr source, whereas the increase in Rp is only 0.003 Ω $cm^2$ for the MP catalyst-coated cathode (**Figure 4**a (iii)). Both BCFN coated LSCF and bare BCFN cathodes show a comparable degradation (increased by ~0.03 Ω $cm^2$ over the 100-h test), higher than that of the MP catalyst-coated LSCF cathode. It indicates that the MP catalyst-coated LSCF cathode has a higher tolerance towards Cr poisoning than BCFN coated LSCF and bare BCFN cathodes. When operated in humidified air with Cr source, the MP catalyst-coated cathode shows a similar degradation rate (0.32% $h^{-1}$) to the $BaCO_3$ coated cathode (0.38% $h^{-1}$, **Figure 4**a (iv)), suggesting that the $BaCO_3$ phase contributes more to the enhanced durability than the BCFN phase. It is notable that the MP catalyst-coated LSCF cathode in this work shows a comparable stability but higher activity compared to the PNM coated LSCF cathode reported previously (**Figure 4**a (iv)).[18] Durability of the MP catalyst-coated LSCF cathode was further investigated at a lower temperature of 650 °C for a longer period of time (500 h). As shown in **Figure S5** and **Figure 4**a, the coated LSCF cathode exhibits a higher stability at 650 °C than that at 750 °C. For example, the degradation rate of the MP catalyst-coated LSCF cathode decreased from $1\times10^{-3}$ to $2.7\times10^{-4}$ Ω $cm^2$ $h^{-1}$ as the operating temperature was reduced from 750 to 650 °C, due partially to the decreased partial pressure of $CrO_2(OH)_2$ at lower temperatures (~0.22 and ~0.09 Pa at 750 and 650 °C, respectively, in wet air with 3 vol.% $H_2O$).[56]

As shown in **Figure 4**b and **Figure S6**, a significant increase in the $R_{IF}$ and $R_{LF}$ is observed for the bare LSCF cathode after the stability test in the presence of Cr. The increased $R_{IF}$ should be attributed to the inert Cr-containing compounds (e.g., $SrCrO_4$, **Figure 4**d and **Figure S7**) formed

on the cathode surface, which blocked the active sites for surface oxygen reactions. The increased $R_{LF}$ should be attributed to the particle coarsening issue (**Figure 4**d), which reduced the porosity of the electrode and limited the mass transfer process. In contrast, the MP catalyst-coated LSCF cathode shows more stable EIS and electrode morphology (**Figure 4**b-e and **Figure S6**). The concentration of Cr in the electrode after the durability test was quantified by analyzing the EDS using an empirical law proposed by Schuler *et al.*[57] The average Cr concentration in the MP catalyst-coated LSCF cathode is about 0.1 at.%, one order of magnitude lower than that of the bare LSCF cathode (3.5 at.% ), confirming the high Cr-tolerance of the MP coating. Energetically favorable Cr-poisoning reactions on the cathode surface are listed in **Table 1** and proposed degradation processes are schematically shown in **Figure 4**f. For the bare LSCF cathode, Sr-O segregations (in the form of $Sr(OH)_2$ in humidified air) on the LSCF surface readily react with Cr species (e.g., $CrO_3$ and $Cr(O_2H)_2$) to form inert $SrCrO_4$, which is detrimental to the ORR activity.[16] Reaction energies of these reactions (S1-S3, **Table 1**) are between -120.5 kJ $mol^{-1}$ and -87 kJ $mol^{-1}$. As for the MP catalyst-coated cathode, the LSCF surface is covered by BCFN and $BaCO_3$ phases. Although Ba-O segregations on the BCFN surface [26, 43] may react with Cr species through reactions S4-S6 (**Table 1**, reaction energies between -148.5 and -103.9 kJ $mol^{-1}$), the $BaCO_3$ phase in the outer layer of the MP coating is almost inert to Cr species due to the low reaction energies between $BaCO_3$ and $Cr_2O_3$ or $Cr(HO_2)_2$ (-29.65 kJ $mol^{-1}$ or -23.35 kJ $mol^{-1}$).

### 2.4. Density functional theory (DFT) calculations

To gain deeper insight into the mechanism of enhancing ORR kinetics and durability of the MP catalyst-coated LSCF cathode, we resorted to DFT-based calculations (**Figure 5** and **Figure S8-10**). **Figure 5**a shows the energy profile of the ORR process on BCFN (001) surface. The $O_2$

adsorption energy on BCFN (001) surface with BaO terminated is -0.56 eV, which is much larger than that on the SrO-terminated LSCF (001) surface (-0.01 eV). The $O_2$ dissociation on BCFN surface (001) is an energetically favorable process with an energy of -0.73 eV, while the surface O diffusion is the rate-determining step, showing a high energy of 0.86 eV (**Figure 5**a). The bulk diffusion barrier of O in the O, Ba-deficient BCFN is much lower than that in the defect-free BCFN (0.5 eV versus 1.1 eV, **Figure 5**a), highlighting the importance of defects of the BCFN phase in the MP catalyst coating. In addition, the BCFN phase exhibits a much lower oxygen vacancy formation energy than LSCF (0.67-0.85 eV versus 1.77 eV, **Table S2**), implying that BCFN is more active for ORR. **Figure 6**b compares the adsorption energy of $CrO_3$ on the surface of LSCF, BCFN, and $BaCO_3$. The highest adsorption energy of -5.07 eV is observed on the LSCF (001) surface, consistent with the rapid degradation in Rp of bare LSCF cathodes shown above. BaO-terminated BCFN (010) surface shows a high $CrO_3$ adsorption energy of -4.59 eV, followed by -3.93 eV for NbCoO-terminated surface, and -2.86 eV for FeCoO-terminated surface. $BaCO_3$ (010) surface shows the highest Cr tolerance with the adsorption energy of -1.84 eV, which is in good agreement with the experimental results.

### 2.5. Performance of Single Cells with the MP catalyst-coated LSCF cathode

Enhanced ORR activity and durability of the MP catalyst-coated cathode were further verified in single cells under practical fuel cell operation conditions. Cross-sectional SEM image of the anode-supported cell with a configuration of Ni-YSZ | YSZ|SDC | MP catalyst-coated LSCF is shown in **Figure 6**a. The cell with a MP catalyst-coated cathode shows a dramatically enhanced performance in all the testing temperature range when using ambient air as the oxidant and humidified $H_2$ (3 vol.%$H_2O$) as the fuel (**Figure 6**b). For instance, at 750 °C, the peak powder

density ($P_{max}$) of the MP catalyst-coated cell is 1.40 W $cm^{-2}$, 2.1 times of that of the cell with a bare LSCF cathode (0.67 W $cm^{-2}$, **Figure 6**c). As observed in **Figure 6**d and **Figure S11**, both cells show a comparable ohmic resistance ($R_{ohm}$) and the main difference in total resistance comes from the polarization resistance, which should be attributed to the catalyst coating on the cathode. **Figure 6**e shows the cell voltage as a function of time at a constant current density of 0.25 A $cm^2$ when the cathode was exposed to air with 3%$H_2O$ and Cr source at 650 °C. Benefiting from the MP catalyst coating, the degradation rate of the cell is reduced from ~0.13% $h^{-1}$ to 0.05% $h^{-1}$. EIS measurements of the cells after the durability test show a more stable polarization resistance of the cell with catalyst coating (**Figure 6**d), confirming the excellent tolerance to $H_2O$ and Cr of the MP catalyst-coated LSCF cathode.

## 3. Conclusion

We have developed an efficient MP catalyst with high electrocatalytic activity for ORR and excellent tolerance to water vapor and Cr poisoning. The MP catalyst-coated LSCF cathode has a very low polarization resistance (Rp ≈ 0.048 Ω $cm^2$ at 650 °C), about one order of magnitude smaller than that of the bare LSCF cathode. The MP catalyst-coated LSCF cathode also exhibits excellent tolerance against $H_2O$ and Cr under typical fuel cell operating conditions. More importantly, single cells with the MP catalyst-coated LSCF cathode demonstrate high peak power density ($P_{max}$ of ~0.49 W $cm^{-2}$ at 650 °C) and significantly enhanced durability (degradation rate of 0.05% $h^{-1}$ at 0.25 A $cm^{-2}$ and 650 °C) when exposed to humidified air with Cr source, much better than the cells with a bare LSCF cathode ($P_{max}$ of ~0.23 W $cm^{-2}$ at 650 °C and degradation rate of 0.13% $h^{-1}$ at 0.25 A $cm^{-2}$ and 650 °C). The high performance is attributed to the improved

ORR activity of the BCFN phase and to the enhanced durability of $BaCO_3$ phase, as confirmed by experimental measurements and DFT-based computations.

## 4. Experimental procedures

### 4.1. Preparation of infiltration solution for surface modification

The infiltration solution was prepared by dissolving a stoichiometric amount of $Ba(NO_3)_2$ (99%, Alfa-Aesar), $Co(NO_3)_2 \cdot 6H_2O$ (99%, Sigma-Aldrich), $Fe(NO_3)_9 \cdot 9H_2O$ (98%, Sigma-Aldrich), and $C_4H_4NNbO_9 \cdot xH_2O$ (98%, Sigma-Aldrich) in deionized water. Citric acid (CA) and polyethylene glycol (PEG) were added as chelating and complexing agents, respectively. The molar ratio between the metal ions, CA, and PEG was 1:1.5:4. 5 wt% polyvinyl pyrrolidone was added to the solution as a surfactant.

### 4.2. Fabrication of symmetrical cells

Symmetrical cells with a configuration of LSCF/SDC/LSCF were prepared by bonding the LSCF ($(La_{0.6}Sr_{0.4})_{0.95}Co_{0.2}Fe_{0.8}O_{3-x}$, Fuelcell Materials, US) green tape onto both sides of a SDC pellet using an SDC slurry. SDC pellets were prepared by die pressing commercial SDC powder (Fuelcell Materials, US), followed by sintering at 1450 °C for 5 hours. LSCF green tapes were prepared by a tape casting method. The cells were then co-fired at 1080 °C for 2 hours to form porous electrodes (with an area of 0.283 $cm^2$). 15 μL of the stock solution (0.1 mol $L^{-1}$) was infiltrated into the porous cathode and then fired for 1 hour at 750 ºC and 950 ºC to form MP catalyst and BCFN single phase catalyst, respectively. Same amount of the $Ba(NO_3)_2$ solution with chelating and complexing agents (0.1 mol $L^{-1}$) was infiltrated and treated at 750 °C for 1 h in air to form $BaCO_3$ coated LSCF for comparison. A commercial Crofer 22 APU, with a chemical composition of 22~24 wt% Cr, 0.3~0.8 wt% Mn, 0.5 wt% Si, 0.5 wt% Al, and 0.5 wt% Cu, etc.,

was used as the Cr source for contamination tests. The Cr-tolerance test set-up and more details can be found in our previous work.[18] The humidified air was introduced to the system by flowing air through a water bubbler at room temperature.

### 4.3. Fabrication of single cells

Single cells with an anode-supported configuration of NiO-YSZ (8 mol% $Y_2O_3$-doped $ZrO_2$)|YSZ|SDC|LSCF were fabricated *via* the same method as described in our previous study.[18] Specifically, a NiO-YSZ anode support was prepared by a tape casting method and pre-fired at 900 ºC for 2 h. The anode functional layer and electrolyte layer were fabricated by a dip-coating process, followed by co-sintering with the anode support at 1400 ºC for 4 h. The SDC barrier layer was fabricated by a dip-coating process and then fired at 1250 ºC for 2 h. The LSCF cathode was brush-painted onto the anode-supported cell and fired at 1080 °C for 2 h. The catalyst coating was prepared using the same procedures for the fabrication of symmetrical cells. The catalyst loading is about 7.5 wt% of the LSCF cathode.

### 4.4. Electrochemical measurements

Polarization resistances of cathodes were measured in a two-electrode symmetrical cell configuration using two pieces of silver mesh as current collectors. Rp was determined by measuring the differences between real axis intercepts in the impedance plot. EIS were measured under a Solartron 1255 HF frequency response analyser interfaced with an EG&G PAR potentiostat model 273A in the frequency range from 100 kHz to 0.1 Hz. Current-Voltage curves of single cells were obtained at 600-750 °C with the anode fueled by a gas mixture of 3 vol.% $H_2O$ and 97 vol.% $H_2$ at a flow rate of 10 sccm. The stability of single cells was monitored using an Arbin multichannel electrochemical testing system.

### 4.5. Characterizations

Microstructure and morphology of the electrode were characterized using a Hitachi SU8010 SEM. The EDS mapping was characterized by Zeiss Ultra60 FE-SEM Ranking with EDS attachment. An FEI Tecnai F30 super-twin field-emission-gun transmission electron microscope operating at 300 kV was used to acquire the TEM images, bright-field scanning TEM images and electron diffraction patterns. The HRTEM images were recorded by a Gatan OneView camera. The EELS was acquired by a Gatan Tridiem 863 UHS GIF system. Raman spectroscopy was performed using a Renishaw RM 1000 Spectro microscopy system equipped with an air-cooled Ar laser (CVI Melles Griot) with a wavelength of 514 nm at a total power of 10 mW. Thermal gravimetric analysis (TGA) was carried out to determine the catalyst loading by using an apparatus of SDTQ-600 (TA Instruments Co.) in air with a heating rate of 5 °C $mim^{-1}$. The Brunauer–Emmett–Teller (BET) used to identify specific surface area and pore size distribution was estimated from the measurement of nitrogen adsorption–desorption isotherm which were carried out on an ASAP 2020 analyzer using nitrogen adsorption-desorption isotherms taken at the boiling point of liquid nitrogen (77K). XRD patterns were recorded from an X′Pert Alpha-1 diffractometer using the Ka1 component of Cu radiation.

### 4.6. Computational method

DFT calculations were performed by using Vienna ab initio simulation package (VASP) with the projector-augmented-wave (PAW) method. Generalized gradient approximation (GGA) with Perdew-Burke-Ernzerhof (PBE) exchange-correlation function and spin-polarization were employed and the cut off energy for PAW is 400 eV. Monkhorst-Pack meshes with (3×3×3) and (2x2x1) were used for bulk $BaCO_3$ (*Pnma*), BCFN ($Ba_8Co_5Fe_2Nb_1O_{24}$, *Pm/3m(221)*) and $La_2Sr_3FeCo_4O_{15}$ (LSCF, *Panma*) and corresponding surface optimization, respectively. A vacuum

slab of 15 Å was used to avoid interactions between different layers. The surface energy for a specific crystalline plane was calculated by $E_{surf}$ = E{surface structure} - E{bulk structure}, where E{surface structure] and E{bulk structure} are the predicted electronic energies for surface and perfect bulk structures. The oxygen-vacancy formation energy ($E_{VO}$) was calculated by $E_{VO}$ = E{defective structure} + 1/2E{$O_2$} – E{perfect structure}, where E{defective surface}, E{perfect surface}, and E{$O_2$} are the predicted electronic energies for defective and perfect bulk structures and $O_2$, respectively. The adsorption energy ($E_{ad}$) of $O_2$ on a surface was calculated by $E_{ad}$ = E{$O_2$-surface} – E{surface} – E{$O_2$}), where E{$O_2$-surface} and E{surface} are the predicted electronic energies for an adsorbed $O_2$ species on a surface and its bare surface. E{$O_2$} is energy for gas-phase oxygen. Bulk diffusion barriers of $E_a$ were determined by the climbing image-nudged elastic band (CI-NEB) method.

**Supporting Information**
Supporting Information is available from the Wiley Online Library or from the author.

**Acknowledgements**

Y.N., Y.Z., and W.L are contributed equally to this work. The work was supported by US Department of Energy (DOE) Solid Oxide Fuel Cell Program (DE-FE0031201), DOE EERE Hydrogen and Fuel Cell R&D Program (DE-EE0008439), the Application Fundamental Research project of Sichuan Province (Grant. No. 2019YJ0169), and the Natural Science foundation of China (Grant. No. 51972043). Y.N. acknowledges the financial support of a scholarship from the China Scholarship Council (Grant No. 201906075015).

Received: ((will be filled in by the editorial staff))
Revised: ((will be filled in by the editorial staff))
Published online: ((will be filled in by the editorial staff))

**References**


[1] D. J. Brett, A. Atkinson, N. P. Brandon, S. J. Skinner, *Chem. Soc. Rev.* **2008**, *37*, 1568.

[2] M. Liu, M. E. Lynch, K. Blinn, F. M. Alamgir, Y. Choi, *Mater. Today* **2011**, *14*, 534.

[3] J. A. Kilner, M. Burriel, *Annu. Rev. Mater. Res.* **2014**, *44*, 365.

[4] A. Tarancón, M. Burriel, J. Santiso, S. J. Skinner, J. A. Kilner, *J. Mater. Chem. A* **2010**, *20*, 3799.

[5] C. Sun, R. Hui, J. Roller, *J. Solid State Electrochem.* **2009**, *14*, 1125.

[6] S. P. Jiang, *Int. J. Hydrogen Energy* **2019**, *44*, 7448.

[7] Y. Li, W. Zhang, Y. Zheng, J. Chen, B. Yu, Y. Chen, M. Liu, *Chem. Soc. Rev.* **2017**, *46*, 6345.

[8] B. Koo, K. Kim, J. K. Kim, H. Kwon, J. W. Han, W. Jung, *Joule* **2018**, *2*, 1476.

[9] D. Oh, D. Gostovic, E. D. Wachsman, *J. Mater. Res.* **2012**, *27*, 1992.

[10] H. Wang, K. J. Yakal-Kremski, T. Yeh, G. M. Rupp, A. Limbeck, J. Fleig, S. A. Barnett, *J. Electrochem. Soc.* **2016**, *163*, F581.

[11] S. P. Simner, M. D. Anderson, M. H. Engelhard, J. W. Stevenson, *Electrochem. Solid-State Lett.* **2006**, *9*, A478.

[12] S. P. Jiang, J. P. Zhang, X. G. Zheng, *J. Eur. Ceram. Soc.* **2002**, *22*, 361.

[13] S. P. Jiang, Y. Zhen, *Solid State Ionics* **2008**, *179*, 1459.

[14] J. W. Fergus, *Int. J. Hydrogen Energy* **2007**, *32*, 3664.

[15] R. A. Budiman, K. D. Bagarinao, S. S. Liu, D. H. Cho, T. Ishiyama, H. Kishimoto, K. Yamaji, T. Horita, H. Yokokawa, *J. Electrochem. Soc.* **2018**, *165*, F1206.

[16] Y. Huang, A. M. Hussain, C. Pellegrinelli, C. Xiong, E. D. Wachsman, *ACS Appl. Mater. Interfaces* **2017**, *9*, 16660.

[17] S. P. Jiang, X. Chen, *Int. J. Hydrogen Energy* **2014**, *39*, 505.

[18] Y. Chen, S. Yoo, X. Li, D. Ding, K. Pei, D. Chen, Y. Ding, B. Zhao, R. Murphy, B. deGlee, J. Liu, M. Liu, *Nano Energy* **2018**, *47*, 474.

[19] M. Kim, H. Muroyama, T. Matsui, K. Eguchi, *J. Electrochem. Soc.* **2019**, *166*, F1269.

[20] M. Niania, R. Podor, T. B. Britton, C. Li, S. J. Cooper, N. Svetkov, S. Skinner, J. Kilner, *J. Mater. Chem. A* **2018**, *6*, 14120.

[21] Q. Zhang, S. Tan, M. Ren, H. Yang, D. Tang, K. Chen, T. Zhang, S. P. Jiang, *J. Power Sources* **2018**, *383*, 34.

[22] D. Ding, X. Li, S. Y. Lai, K. Gerdes, M. Liu, *Energy Environ. Sci.* **2014**, *7*, 552.

[23] D. Ding, M. Liu, Z. Liu, X. Li, K. Blinn, X. Zhu, M. Liu, *Adv. Energy Mater.* **2013**, *3*, 1149.

[24] K. Chen, N. Ai, K. M. O'Donnell, S. P. Jiang, *Phys. Chem. Chem. Phys.* **2015**, *17*, 4870.

[25] Y. Chen, S. Yoo, W. Zhang, J. H. Kim, Y. Zhou, K. Pei, N. Kane, B. Zhao, R. Murphy, Y. Choi, M. Liu, *ACS Catal.* **2019**, *9*, 7137.

[26] J. Li, J. Li, D. Yan, J. Pu, B. Chi, L. Jian, *Electrochimica Acta* **2018**, *270*, 294.

[27] K. Pei, Y. Zhou, K. Xu, Z. He, Y. Chen, W. Zhang, S. Yoo, B. Zhao, W. Yuan, M. Liu, Y. Chen, *Nano Energy* **2020**, *72*, 104704.

[28] C. C. Wang, D. Luo, S. P. Jiang, B. Lin, *J. Phys. D: Appl. Phys.* **2018**, *51*, 435502.

[29] M. K. Stodolny, B. A. Boukamp, D. H. A. Blank, F. P. F. van Berkel, *J. Power Sources* **2012**, *209*, 120.

[30] Y. Yu, K. F. Ludwig, J. C. Woicik, S. Gopalan, U. B. Pal, T. C. Kaspar, S. N. Basu, *ACS Appl. Mater. Interfaces* **2016**, *8*, 26704.

[31] L. Zhao, S. Amarasinghe, S. P. Jiang, *Electrochem. Commun.* **2013**, *37*, 84.

[32] L. Nie, M. Liu, Y. Zhang, M. Liu, *J. Power Sources* **2010**, *195*, 4704.

[33] L. dos Santos-Gómez, J. M. Porras-Vázquez, E. R. Losilla, F. Martín, J. R. Ramos-Barrado, D. Marrero-López, *J. Power Sources* **2017**, *347*, 178.

[34] X. Lou, S. Wang, Z. Liu, L. Yang, M. Liu, *Solid State Ionics* **2009**, *180*, 1285.

[35] T. Hong, K. S. Brinkman, C. Xia, *ChemElectroChem* **2016**, *3*, 805.

[36] F. Fang, N. Feng, P. Zhao, C. Chen, X. Li, J. Meng, G. Liu, L. Chen, H. Wan, G. Guan, *Chem. Eng. J.* **2019**, *372*, 752.

[37] X. Jiang, Y. Shi, W. Zhou, X. Li, Z. Su, S. Pang, L. Jiang, *J. Power Sources* **2014**, *272*, 371.

[38] B. C. H. Steele, *Solid State Ionics* **1996**, *86-88*, 1223.

[39] Y. Chen, Y. Chen, D. Ding, Y. Ding, Y. Choi, L. Zhang, S. Yoo, D. Chen, B. deGlee, H. Xu, Q. Lu, B. Zhao, G. Vardar, J. Wang, H. Bluhm, E. J. Crumlin, C. Yang, J. Liu, B. Yildiz, M. Liu, *Energy Environ. Sci.* **2017**, *10*, 964.

[40] Y. Chen, Y. Choi, S. Yoo, Y. Ding, R. Yan, K. Pei, C. Qu, L. Zhang, I. Chang, B. Zhao, Y. Zhang, H. Chen, Y. Chen, C. Yang, B. deGlee, R. Murphy, J. Liu, M. Liu, *Joule* **2018**, *2*, 938.

[41] T. Yang, Y. Wen, T. Wu, N. Xu, K. Huang, *J. Mater. Chem. A* **2020**, *8*, 82.

[42] C. S. Tu, R. R. Chien, V. H. Schmidt, S. C. Lee, C. C. Huang, C. L. Tsai, *J. Appl. Phys.* **2009**, *105*, 103504.

[43] J. Wang, Z. Yang, K. Yang, Y. Chen, X. Xiong, S. Peng, *Electrochimica Acta* **2018**, *289*, 503.

[44] J. Cui, J. Wang, W. Fan, Y. Wan, X. Zhang, G. Li, K. Wu, Y. Cheng, J. Zhou, *Int. J. Hydrogen Energy* **2017**, *42*, 20164.

[45] B. Huang, C. H. Bartholomew, B. F. Woodfield, *Microporous Mesoporous Mater.* **2014**, *184*, 112.

[46] A. P. B. Selvadurai, V. Pazhanivelu, C. Jagadeeshwaran, R. Murugaraj, I. Panneer Muthuselvam, F. C. Chou, P. M. Md Gazzali, G. Chandrasekaran, *J. Sol-Gel Sci. Technol.* **2016**, *80*, 827.

[47] S. P. Jiang, *Int. J. Hydrogen Energy* **2012**, *37*, 449.

[48] Y. Chen, S. Yoo, Y. Choi, J. H. Kim, Y. Ding, K. Pei, R. Murphy, Y. Zhang, B. Zhao, W. Zhang, H. Chen, Y. Chen, W. Yuan, C. Yang, M. Liu, *Energy Environ. Sci.* **2018**, *11*, 2458.

[49] M. Li, Z. Sun, W. Yang, T. Hong, Z. Zhu, Y. Zhang, X. Wu, C. Xia, *Phys. Chem. Chem. Phys.* **2016**, *19*, 503.

[50] J. Mizusaki, K. Amano, S. Yamauchi, K. Fueki, *Solid State Ionics* **1987**, *22*, 313.

[51] H. Zhu, R. J. Kee, V. M. Janardhanan, O. Deutschmann, D. G. Goodwin, *Journal of The Electrochemical Society* **2005**, *152*.

[52] Kestell, Virginia Polytechnic Institute and State University (Blacksburg, Virginia), **2010**.

[53] E. Siebert, A. Hammouche, M. Kleitz, *Electrochimica Acta* **1995**, *40*, 1741.

[54] Y. Takeda, R. Kanno, M. Noda, Y. Tomida, O. Yamamoto, *J. Electrochem. Soc.* **1987**, *134*, 2656.

[55] M. J. Escudero, A. Aguadero, J. A. Alonso, L. Daza, *Journal of Electroanalytical Chemistry* **2007**, *611*.

[56] X. Chen, Y. Zhen, J. Li, S. P. Jiang, *Int. J. Hydrogen Energy* **2010**, *35*, 2477.

[57] J. Andreas Schuler, P. Tanasini, A. Hessler-Wyser, J. V. herle, *Scr. Mater.* **2010**, *63*, 895.

[58] M. Sahibzada, S. J. Benson, R. A. Rudkin, J. A. Kilner, *Solid State Ionics* **1998**, *113-115*, 285.

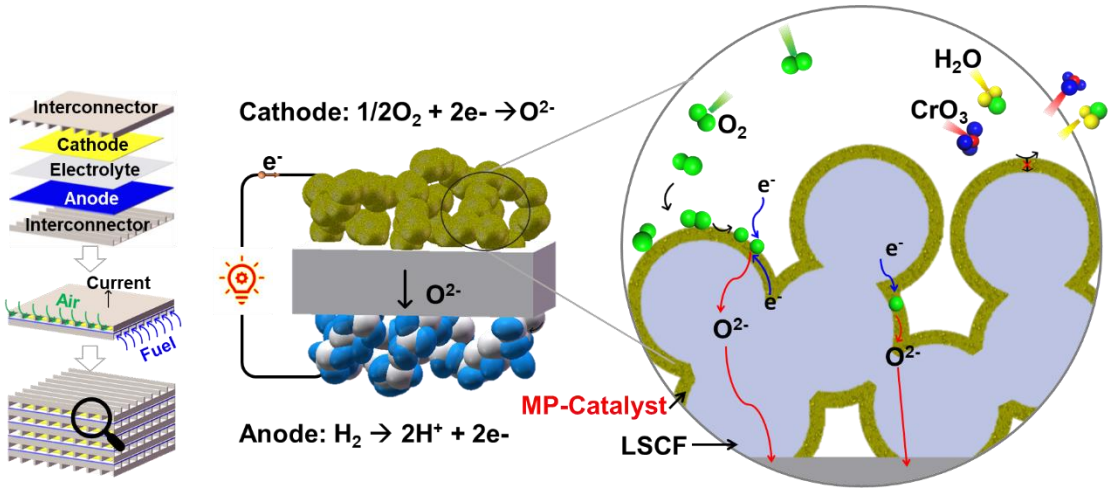


**Figure 1.** Schematic illustration of a fuel cell stack with the MP catalyst-coated LSCF cathode, which has enhanced ORR activity and improved tolerance to contaminants (Cr and $H_2O$).

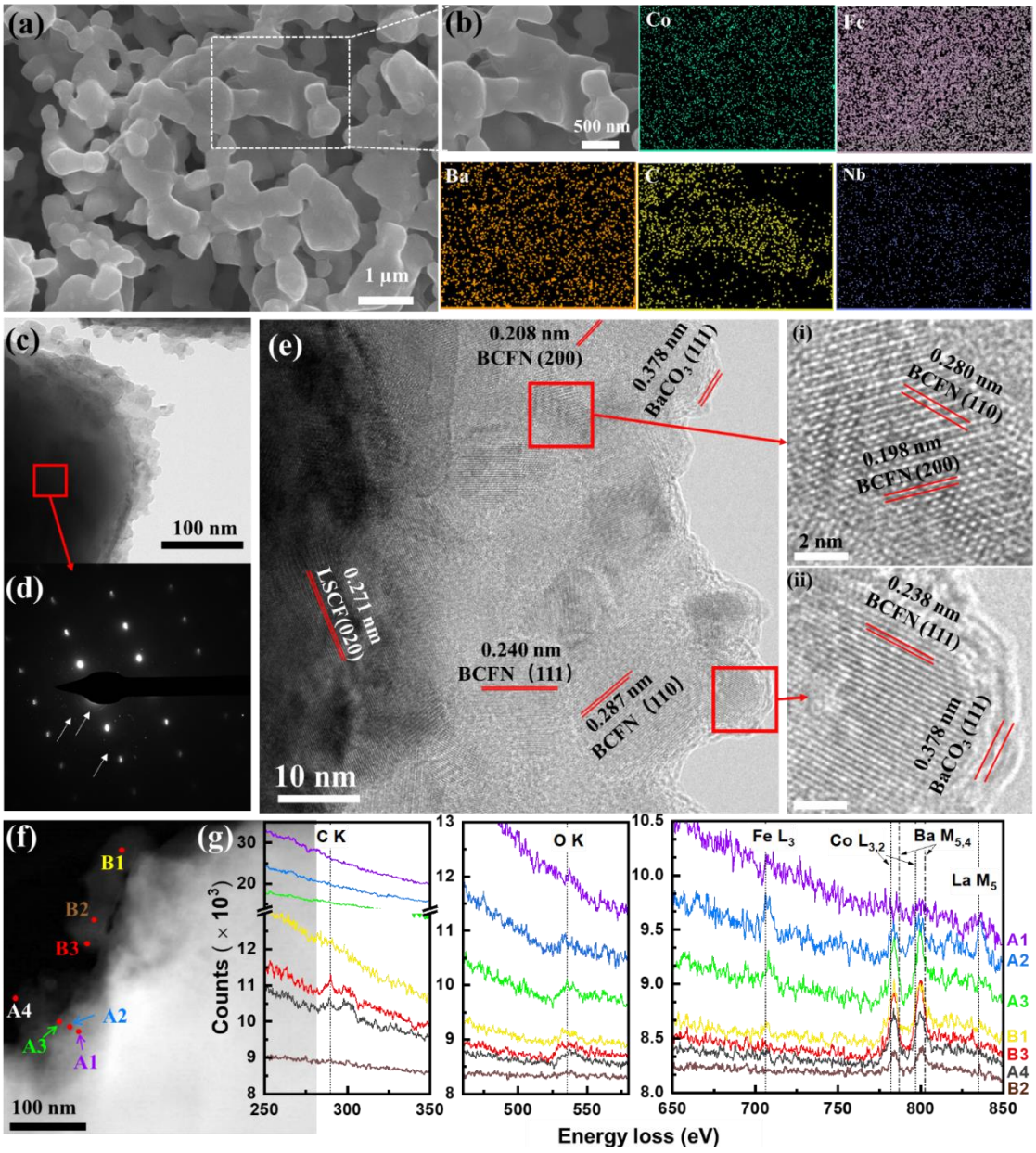


**Figure 2.** Morphology and structure of the MP catalyst-coated LSCF. **(a)** SEM image of the MP catalyst-coated LSCF electrode. **(b)** SEM image and EDS mapping of the MP catalyst-coated LSCF electrode. **(c)** Bright-field TEM image of the MP catalyst-coated LSCF grain. **(d)** SAED patterns recorded from the area marked in (c). **(e)** HR-TEM images of the MP catalyst-coated LSCF grain and the zoomed-in areas: (i) and (ii). **(f)** Bright-field TEM image of the MP catalyst-coated LSCF grain with the marked areas for EELS scanning. **(g)** EELS spectra of the areas in (e) showing C K, O K, Fe $L_3$, Co $L_{3,2}$, Ba $M_{5,4}$ and La $M_5$ edges.

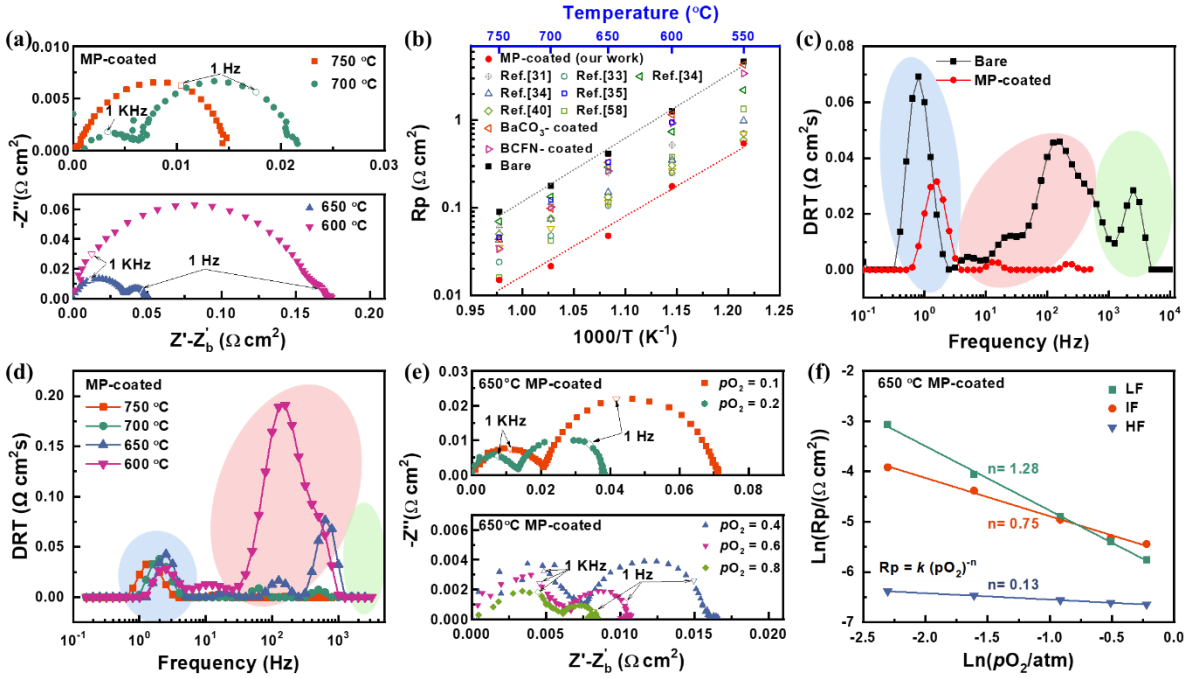


**Figure 3.** EIS and DRT analysis of bare LSCF and MP catalyst-coated LSCF electrodes. **(a)** Nyquist plots of the MP catalyst-coated LSCF electrode tested at different temperatures. **(b)** Temperature dependence of Rps of the bare LSCF electrode and catalysts coated LSCF electrodes. Reported Pd[58], GDC[31, 33], SSC[34], LSCF[34], $BaCO_3$[35], and PBCC with PrO*x* and $BaCoO_{3-\delta}$[40] coated LSCF electrodes were added for comparison from references [31, 33-35, 40, 58]. **(c)** DRT functions of the bare LSCF and MP catalyst-coated LSCF electrodes at 750 °C. **(d)** DRT analysis of the MP catalyst-coated LSCF electrode at 600-750 °C. **(e)** Nyquist plots of the MP catalyst-coated LSCF electrode at 650°C under different $p_{O_2}$. **(f)** $p_{O_2}$ dependence of Rps of the MP catalyst-coated LSCF electrode at 650 °C.

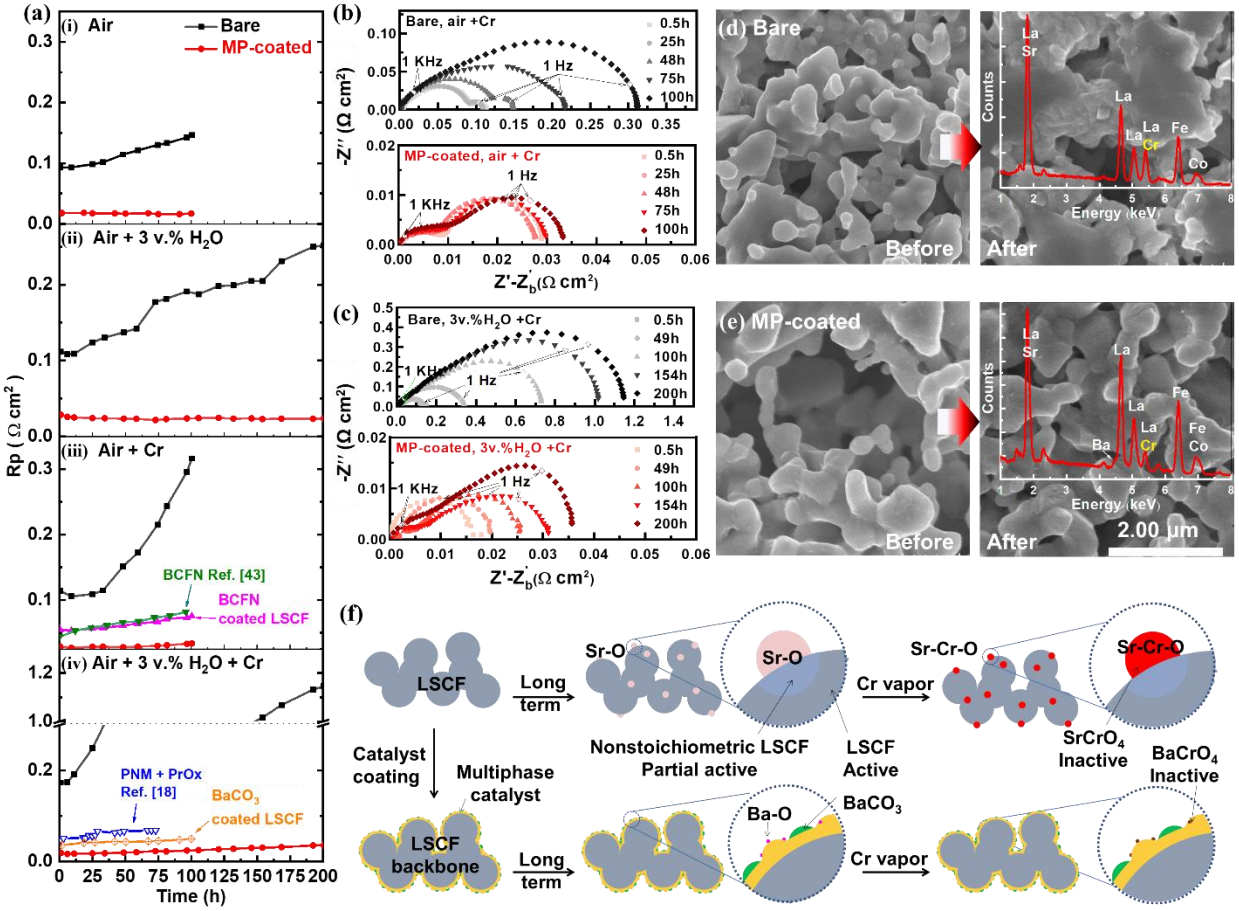


**Figure 4.** **(a)** Polarization resistance (Rp) of bare LSCF and catalyst coated LSCF electrodes as a function of time, measured under open circuit voltage (OCV) conditions at 750 °C in (i) dry air, (ii) dry air with the presence of Cr source, (iii) 3% $H_2O$ humidified air, and (iv) 3% $H_2O$ humidified air with the presence of Cr source. BCFN cathode and PNM-PrO*x* coated LSCF cathode from Ref.[43] and Ref.[18], respectively, were added for comparison. **(b)** EIS curves of bare LSCF and MP catalyst-coated LSCF electrodes measured at different time at 750 °C in dry air with the presence of Cr source. **(c)** EIS curves of bare LSCF and MP catalyst-coated LSCF electrodes measured at different time at 750 °C in 3% $H_2O$ humidified air with the presence of Cr source. **(d)** SEM images and EDS of the bare LSCF electrode before and after the 100 h-durability test in dry air with the presence of Cr source at 750 °C. **(e)** SEM images and EDS of the MP catalyst-coated LSCF electrode before and after the 100 h-durability test in dry air with the presence of Cr source at 750 °C. **(f)** Schematic illustration of the surface evolution of the bare LSCF and MP catalyst-coated LSCF electrodes during the long-term operation with the presence of Cr source. The yellow and green zones represent $Ba_{1-x}Co_{0.7}Fe_{0.2}Nb_{0.1}O_{3-\delta}$ and $BaCO_3$, respectively.

**Table 1.** The probable Cr-poisoning reactions and reaction energies.

| No. | Reaction Equation (normalized to reflect molar fraction) | $E_{rxn}$ of eqn (kJ/mol) | $E_{rxn}$/atom (eV/atom) |
|---|---|---|---|
| S1 | $0.5\ SrO + 0.5\ CrO_3 \rightarrow 0.5\ SrCrO_4$ | -120.5 | -0.416 |
| S2 | $0.5\ Sr(OH)_2 + 0.5\ CrO_3 \rightarrow 0.5\ SrCrO_4 + 0.5\ H_2O$ | -93.03 | -0.214 |
| S3 | $0.5\ Sr(OH)_2 + 0.5\ CrO_2(OH)_2 \rightarrow 0.5\ SrCrO_4 + H_2O$ | -86.73 | -0.150 |
| S4 | $0.5\ BaO + 0.5\ CrO_3 \rightarrow 0.5\ BaCrO_4$ | -148.5 | -0.513 |
| S5 | $0.5\ Ba(OH)_2 + 0.5\ CrO_3 \rightarrow 0.5\ BaCrO_4 + 0.5\ H_2O$ | -110.2 | -0.254 |
| S6 | $0.5\ Ba(OH)_2 + 0.5\ CrO_2(OH)_2 \rightarrow 0.5\ BaCrO_4 + H_2O$ | -103.9 | -0.179 |
| S7 | $0.5\ BaCO_3 + 0.5\ CrO_3 \rightarrow 0.5\ BaCrO_4 + 0.5\ CO_2$ | -29.65 | -0.068 |
| S8 | $0.5\ BaCO_3 + 0.5\ Cr(HO_2)_2 \rightarrow 0.5\ BaCrO_4 + 0.5\ CO_2 + 0.5\ H_2O$ | -23.35 | -0.040 |

[a] The data above is reproduced from https://materialsproject.org/;
[b] $E_{rxn}$ of eqn represents the reaction energy per mol of the displayed reaction equation;
[c] $E_{rxn}$ / atom represents the reaction energy normalized by the total number of reactant atoms.

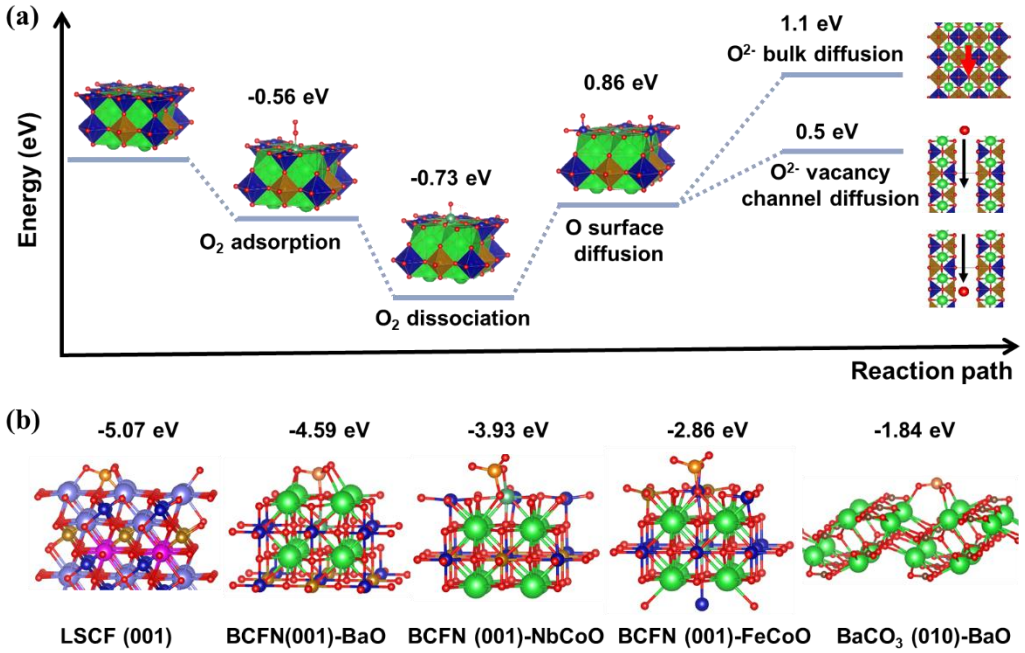


**Figure 5.** Unravelling the mechanism of enhancing ORR activity and stability of the LSCF cathode by a MP catalyst coating. **(a)** Schematic illustration of the energy profile for the ORR on a BCFN (010) surface. **(b)** Optimized structures and adsorption energies of $CrO_3$ on the surface of LSCF (001), BCFN (001)-BaO, BCFN (001)-NbCoO, BCFN (001)-FeCoO, and $BaCO_3$ (010). The balls with different colors represent: red: O, green: Ba, grey: C, blue: Co, light blue: Nb, brown: Fe, orange: Cr, pink: La, and purple: Sr.

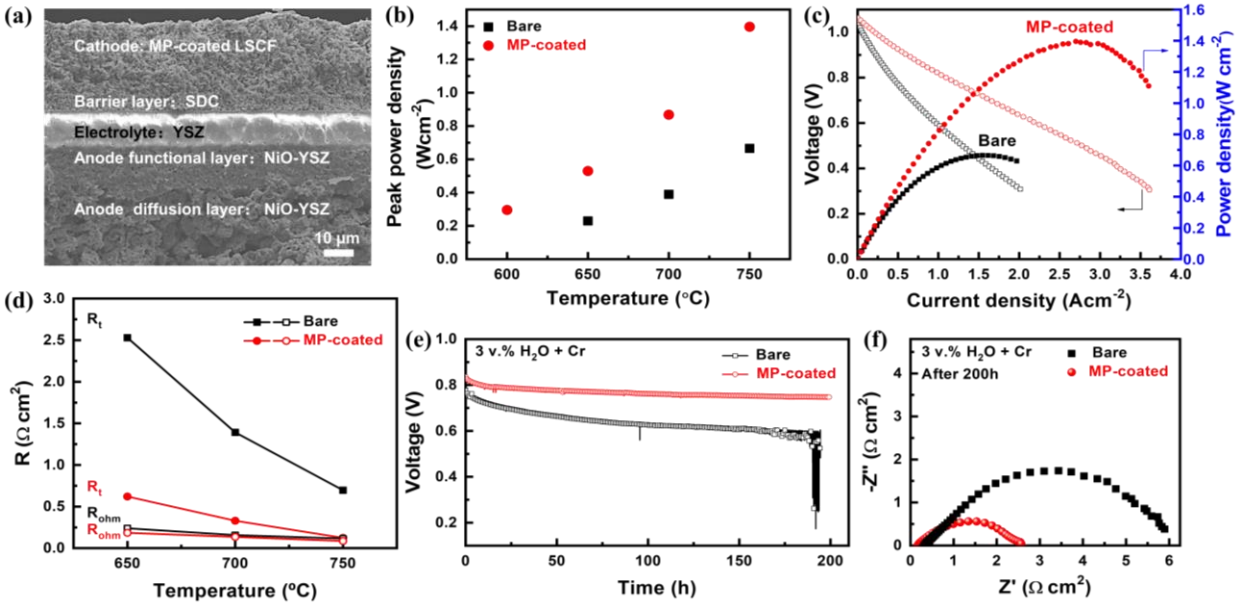


**Figure 6.** Morphology and electrochemical performances of single cells. **(a)** SEM image of the NiO-YSZ/YSZ/SDC/MP catalyst-coated LSCF single cell. **(b)** Peak power densities of the cell with a bare LSCF or MP catalyst-coated LSCF cathode at 600-750 °C using 3%$H_2O$ humidified $H_2$ as the fuel and ambient air as the oxidant. **(c)** Typical current-voltage-peak power (I–V–P) curves of the cell with a bare LSCF or MP catalyst-coated LSCF cathode at 750 °C. **(d)** $R_t$ and $R_{ohm}$ of the cell with a bare LSCF or MP catalyst-coated LSCF cathode at 600-750 °C under OCV conditions **(e)** Durability test of the cells with 3%$H_2O$ humidified air and Cr source in the cathode side at 0.25 A $cm^2$ and 650 °C. **(f)** EIS curves of the cells after the 200 h-durability test.

**A multiphase catalyst-coated LSCF** cathode is developed for intermediate temperature solid oxide fuel cells, demonstrating exceptional ORR activity and excellent stability against $H_2O$ and Cr.

**Keywords**: Multi-phase catalyst, Oxygen reduction reaction, Solid oxide fuel cell, Cr tolerance, Cathode

*Yinghua Niu*[†], *Yucun Zhou*[†], *Weiqiang Lv*[†], *Yu Chen*, Yanxiang Zhang, Weilin Zhang, Zheyu Luo, Nicholas Kane, Yong Ding, Luke Soule, Yuchen Liu, Weidong He*, Meilin Liu**

**Enhancing Oxygen Reduction Activity and Cr Tolerance of Solid Oxide Fuel Cell Cathodes by a Multi-phase Catalyst Coating**

ToC figure